Three-Phase to Single-Phase Multiresonant Direct AC–AC Converter for Metal Hardening High-Frequency Induction Heating Applications

Ryosuke Kawashima, Tomokazu Mishima, *Senior Member, IEEE*, and Chiaki Ide

***Abstract*—A new multiresonant three-phase utility frequency ac (UFAC) to high-frequency ac (HFAC) direct power converter for the industrial metal hardening induction heating (IH) applications is presented in this article. The proposed ac–ac converter features direct frequency conversion with the wide range of soft switching by means of the minimized numbers of bidirectional switches. The conducting current of bidirectional switches can be reduced effectively owing to the multiresonant tank while keeping a high power in the IH load. Accordingly, the practical power converter with simplicity, cost-effectiveness, and high efficiency can be realized on the basis of a simple pulse-frequency modulation (PFM). The circuit topology and operating principle of the proposed converter are described, after which the design procedure of the multiresonant tank and switching frequency is presented. The performances on the soft switching and the steady-state PFM characteristics of the ac–ac converter are evaluated in experiment with the 1.7 kW/85–90-kHz prototype. Finally, the feasibility of the proposed ac–ac converter is evaluated from a practical view point.**

***Index Terms*—Direct ac–ac converter, high-frequency induction heating (IH), pulse-frequency modulation (PFM), series–parallel resonance, zero-current soft switching (ZCS), zero-voltage soft switching (ZVS).**

I. Introduction

HIGH-FREQUENCY Induction heating (IH) systems have been widespread in the industrial fields from the viewpoint of heating efficiency and pollution-free, and the surface hardening and tempering treatment of metals has been contributing greatly to the improvements of the quality of steel machine parts [1]–[4]. It is essential to design the high-frequency generator precisely by taking the skin effect and surface depth of heating into account for effective heating of metal objectives. Fig. 1 illustrates the principle of high-frequency IH for the metal surface treatment, whereby a high-frequency current contributes for a surface hardening of the heating object.

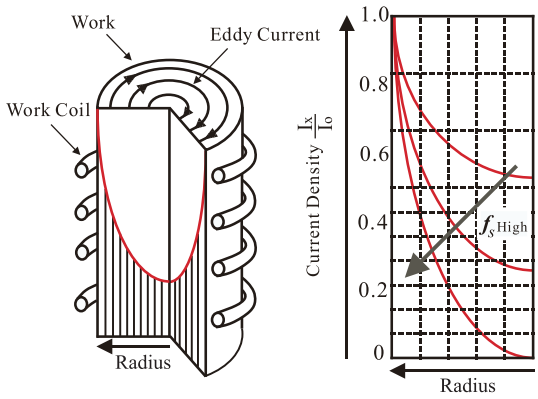

Fig. 1. Skin effect of the metal surface treatment by IH.

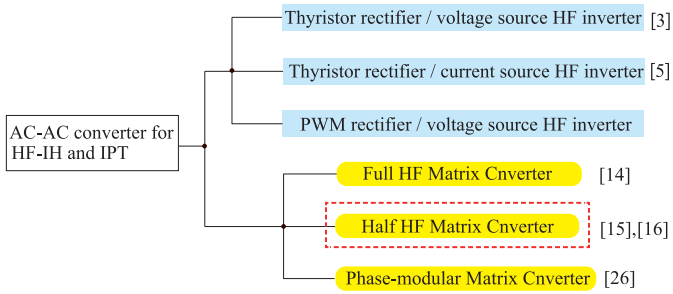

Fig. 2. Classification on the three-phase to single-phase ac–ac converters for IH and IPT systems.

The power stage from the three-phase utility frequency ac (UFAC) to a single-phase high-frequency ac (HFAC) plays a key role for attaining high-efficiency and high performance of the IH and the relevant inductive power transfer (IPT) applications. Fig. 2 shows classification of the three-phase to single-phase ac–ac converters for the IPT systems. The popular and basic circuit topologies for industrial IH applications are composed of three-phase thyristor rectifier and current-source or voltage-source high-frequency inverter (CS HF-INV/VS HF-INV), as depicted in Fig. 3(a)–(c). Those conventional IH systems face with a technical issue of improvements of power density and efficiency due to bulky capacitor and inductor in

Manuscript received December 29, 2019; revised March 13, 2020 and April 28, 2020; accepted June 4, 2020. Date of publication June 16, 2020; date of current version September 4, 2020. This work was supported by the Adaptable and Seamless Technology transfer Program (A-STEP) from Japan Science and Technology Agency (JST), under Grant VP30118067656. Recommended for publication by Associate Editor M. Amirabadi. This work was presented in part at the 11th IEEE Energy Conversion Congress and Expositions, Baltimore, MD, USA, September 29–October 3, 2019. *(Corresponding author: Tomokazu Mishima.)*

Ryosuke Kawashima and Tomokazu Mishima are with the Department of Marine Engineering Graduate School of Maritime Sciences, Kobe University, Hyogo 658-0022, Japan (e-mail: 183w507w@stu.kobe-u.ac.jp; mishima@maritime.kobe-u.ac.jp).

Chiaki Ide is with the Fuji Electronics industry Company Ltd., Osaka 581-0092, Japan (e-mail: chiaki-ide@fujidenshi.co.jp).

Color versions of one or more of the figures in this article are available online at https://ieeexplore.ieee.org.

Digital Object Identifier 10.1109/TPEL.2020.3003026

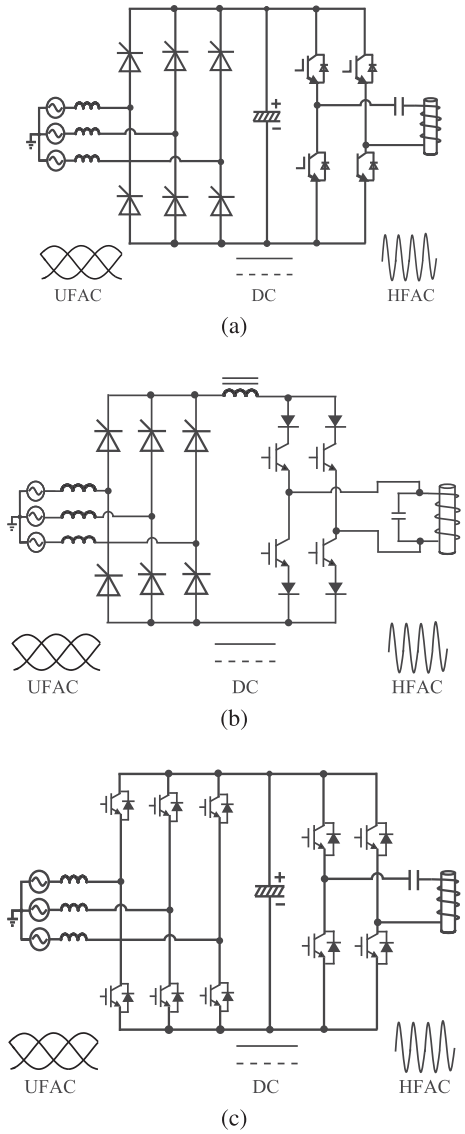

Fig. 3. Conventional two-stage power conversion topologies for IH system. (a) Thyristor rectifier and voltage-source HF inverter [3]. (b) Thyristor rectifier and current-source HF inverter [5]. (c) PWM rectifier and voltage-source HF inverter [6].

the dc link, which causes large volume and short life-cycle of the entire system[2], [3], [5], [6].

A direct ac–ac power conversion (or matrix converter) is considered as a promising candidate for solving the technical problems of a conventional multistage ac–dc–ac power converter [7]. Three-phase to three-phase ac–ac converters [8]–[11], three-phase to single-phase ac–ac converters [12]–[16], single-phase to single-phase ac–ac converters [17]–[22], and three-phase to dc converters [23]–[25] have been proposed for industrial and industrious applications such as battery chargers, ac motor drives, IH and IPT systems.

By spotlighting on the three-phase to single-phase ac–ac converters for IH and IPT applications as treated in this article, the existing and previously developed ac–ac converters can be categorized in Fig. 2. The full high-frequency matrix converter (HF-MC) with the six sets of bidirectional switches has

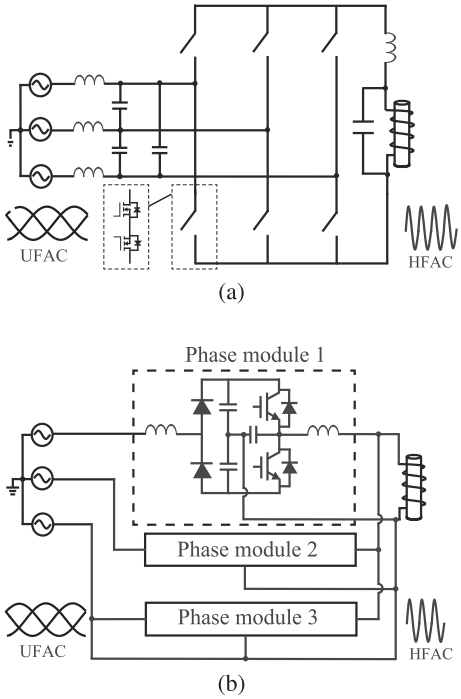

Fig. 4. HF-MCs for the IH system. (a) Full HF-MC [14]. (b) Phase-modular HF-MC [26].

been developed for the high-frequency IH system, as displayed in Fig. 4(a) [14]. However, synchronization of instantaneous currents between the input and output sides is inevitably necessary for power factor correction (PFC) in the line currents, which involves with a complicated commutation process of switching power devices. Furthermore, the critical issue of this topology is that no effective way exists to attain soft commutation in the bidirectional switches over the wide range of load power and source voltage amplitude.

As an another approach of a direct power conversion without any bidirectional switch, a phase-modular three-phase ac to single-phase ac converter has been proposed for a fluid heat exchanger, whereas a combination of three independent single-phase to single-phase ac–ac converters are connected in parallel, as shown in Fig. 4(b) [26]. Thus, development of a direct three-phase to single ac–ac converter applicable to a world-wide three-phase ac power source is still challenging in the industry of induction heaters while minimizing the numbers of circuit components.

Prior to the advent of HF-MC, the simpler topologies while keeping the thee-phase to single-phase direct power conversion for induction heaters, which is named as a "high-frequency cycloconverter," were developed in the past decades [12], [13]. However, the high-frequency cycloconverter is comprised by thyristors with antiparallel diodes; accordingly, the output frequency is inherently limited in the lower than 10 kHz. This kind of the thyristor-based three-phase to single-phase direct power cannot accommodate a modern industrial IH system which demands a 100 kHz and more output frequency.

Meanwhile, metal-oxide-semiconductor gate transistor-based half HF-MCs for IPT applications have also been proposed by

now, which can generate a high-frequency current (no more than 50 kHz) by series resonance with six unidirectional discrete power devices (reversely blocking insulated gate bipolar transistor; RB-IGBT) and one or two switches for power regulations in [15], and six bidirectional switches in [16]. Although the direct power conversion attains successfully, the power control performance significantly depends on a complicated algorithm of pulse modulation and calculation of control variable, accordingly the feasibility of the converter topologies is limited in the middle frequency 20–50 kHz at the current stage of researches and developments.

As a solution for those technical challenges of the existing direct ac–ac converters, a new multiresonant direct ac–ac converter for IH application is proposed in this article [27]. The proposed converter enables the direct three-phase to single-phase conversion by using only three bidirectional switches of two series-connected discrete power MOSFETs, and supplies a large current to the load while suppressing the peak conduction current of switches with the aids of a multiresonant tank. This multiresonant tank in the proposed converter has advantages over the conventional series, parallel, or series–parallel resonant tanks in terms of effective reduction of the inductance in the IH load with a high-frequency switching. The multiresonant tank assists zero-current soft-switching (ZCS) commutations and zero-voltage soft-switching (ZVS) commutation between two-phase bidirectional switches. In addition, the switching pulses of all the bidirectional switches can be implemented with a simple logic circuit, thereby a switching frequency can be raised effectively up to the practical level of metal surface treatments. Accordingly, the output power can be regulated by a narrow frequency variation in PFM with the impedance characteristics of the multiresonant tank. The proposed converter features the cost-effect circuit topology and controller scheme by paying for nonunity power factor in the line currents. The relevant harmonics has no significant impact on the main circuit and controller, and is an acceptable level for an industrial IH application unless the distorted line current flows into a power feeder in a factory.

The rest of this article is organized as follows. The proposed circuit topology and operating principle are described in Section II. The design procedure of the multiresonant tank and resonant frequencies are described in Section III. Performances of the proposed converter are demonstrated by a 1.7 kW–90 kHz prototype in Section IV and its feasibility is verified by the experimental results. In addition, the comparison between the existing three-phase to single-phase ac–ac converters and proposed converter is discussed in Section IV. Finally, the essential performances of the proposed direct ac–ac converter are summarized in Section V.

II. Circuit Topology and Operations

A. Circuit Configuration With Multiresonant Tank

The circuit diagram of the proposed direct ac–ac converter is illustrated in Fig. 5. The three-phase UFAC source is connected with a half HF-MC to feeding power to the single-phase HFAC

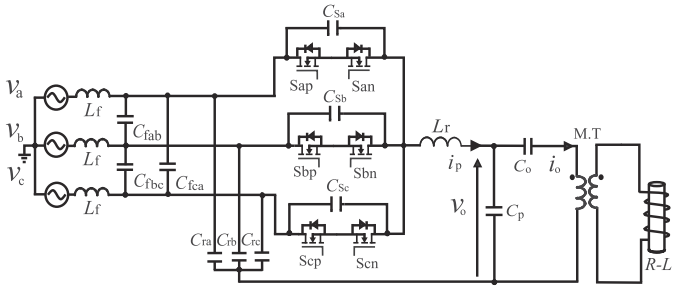

Fig. 5. Proposed three-phase to single-phase direct ac–ac converter with a multiresonant tank for the high-frequency IH systems.

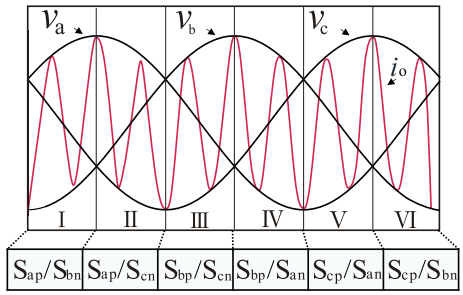

Fig. 6. Six divisions in the three-phase source voltages and the selected active switches.

IH load via an impedance matching transformer (M.T.). The conducting current through the bidirectional switches can be reduced effectively with the aid of the multiresonant tank.

The primary transformer-windings current i_p is generated by the series-resonant tank that consists of L_r and three sets of series capacitor C_r. The load resonant tank is composed of IH load (R–L), series capacitor C_o, and power factor-tuned capacitor C_p. The capacitor C_o has the function of reducing the reactive current by creating series resonance with the load inductance L_o, and suppress the impedance of the parallel-resonant circuit under the condition of high-frequency switching.

The positive switches $S_{\rm mp}$ ($m = \{a, b, c\}$) are commutated by ZVS turn-OFF with assists of lossless snubber capacitors $C_{\rm sa}$, $C_{\rm sb}$, and $C_{\rm sc}$ while ZCS turn-ON operation achieves by the current blocking function of negative switches $S_{\rm mn}$ for the high-frequency positive half-cycle interval. The gate turn-ON/OFF timings are determined under the principle of two-phase modulation that utilizes the maximum voltage and the minimum voltage of the three-phase power source. Accordingly, the switches connected to the maximum and minimum voltage phases in each section are driven interchangeably while those connected to the intermediate voltage phase are rest in switching. The three sets of bidirectional switches are commutated by every one-sixth interval of the UFAC source voltage. Now, consider sector-I of the three-phase voltage waveforms in Fig. 6. Since v_a is the maximum and v_b is the minimum UFAC voltage, the switches $S_{\rm ap}$ and $S_{\rm bn}$ are selected as the two-phase active switches.

Fig. 7 represents the equivalent circuit of the M.T. and IH load. The relevant parameters of the model are obtained by substantially measuring the primary-side voltage v_1 and current

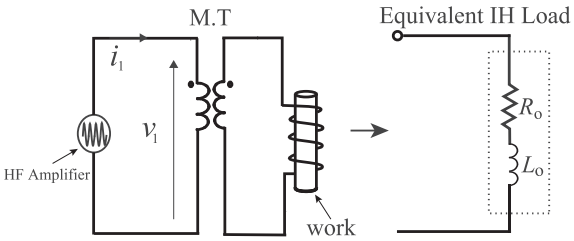

Fig. 7. Equivalent circuit of the M.T. and IH load in the impedance measurement.

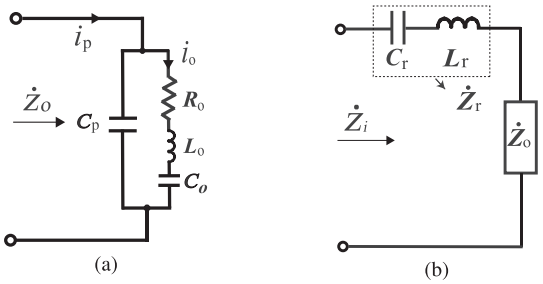

Fig. 8. Modeling of the multiresonant tank and load. (a) Parallel capacitor and equivalent inductive load. (b) With series-resonant tank.

i_1 with respect to the angular switching frequency ω_s $(= 2\pi f_s)$. In the first place, the load impedance $Z_{\rm rms}$ is defined by

$$Z_{\rm rms} = \frac{V_{1\rm rms}}{I_{1\rm rms}} = \sqrt{{R_o}^2 + (\omega_s L_o)^2} \tag{1}$$

$$\cos\theta = \frac{R_o}{\sqrt{{R_o}^2 + (\omega_s L_o)^2}} \tag{2}$$

$$\sin\theta = \frac{\omega_s L_o}{\sqrt{{R_o}^2 + (\omega_s L_o)^2}}. \tag{3}$$

Then, the equivalent circuit parameters of the IH load (R_o, L_o) can be expressed as

$$R_o = Z_{\rm rms} \cdot \cos\theta \tag{4}$$

$$L_o = \frac{Z_{\rm rms}}{\omega_s} \cdot \sin\theta. \tag{5}$$

The multiresonant tank including IH load is shown in Fig. 8(a). The impedance Z_o is given as

$$\dot{Z}_o = \frac{R_o}{(1-\omega_s{}^2 L_o C_p + \frac{C_p}{C_o})^2 + (\omega_s C_p R_o)^2} + j\frac{(\omega_s L_o - \frac{1}{\omega_s C_o})(1-\omega_s{}^2 L_o C_p + \frac{C_p}{C_o}) - \omega_s C_o R_o^2}{(1-\omega_s{}^2 L_o C_p + \frac{C_p}{C_o})^2 + (\omega_s C_p R_o)^2}. \tag{6}$$

The resonant frequencies of the multiresonant tank can be obtained from the imaginary part of (6); the resonant frequency f_{r1} is determined by (R_o–L_o–C_o) while the other resonant frequency f_{r2} is decided by the entire load resonant tank (C_p–R_o–L_o–C_o). Since the resistivity of the high-frequency IH load

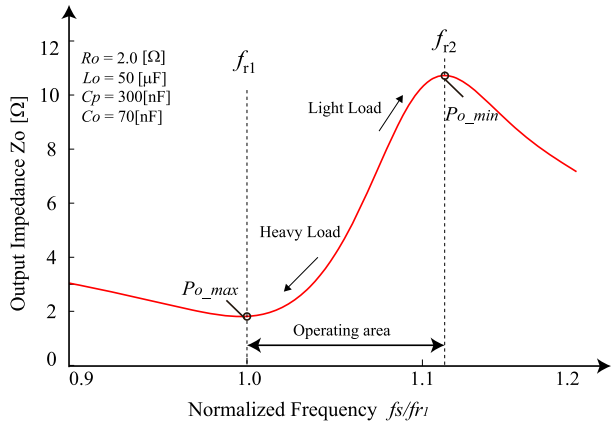

Fig. 9. Characteristic of the output impedance versus normalized frequency.

is relatively small, the resistance R_o can be omitted in (6) to satisfy by

$$\mathrm{Im}(\dot{Z}_o) \simeq \frac{(\omega_s L_o - \frac{1}{\omega_s C_o})(1-\omega_s{}^2 L_o C_p + \frac{C_p}{C_o})}{(1-\omega_s{}^2 L_o C_p + \frac{C_p}{C_o})^2 + (\omega_s C_p R_o)^2} = 0. \tag{7}$$

As a result, the resonant frequencies f_{r1}, f_{r2} can be defined as

$$f_{r1} = \frac{1}{2\pi\sqrt{L_o C_o}} \tag{8}$$

$$f_{r2} = \frac{1}{2\pi}\sqrt{\frac{1}{L_o C_o} + \frac{1}{L_o C_p}} > f_{r1}. \tag{9}$$

Fig. 8(b) represents the equivalent series-resonant tank that is composed of L_r–C_r and Z_o. The series-resonant tank Z_r is defined as

$$\dot{Z}_r = j\left(\omega_s L_r - \frac{1}{\omega_s C_r}\right). \tag{10}$$

Then, the series-resonant frequency $f_{\rm rs}$ can be expressed by

$$f_{\rm rs} = \frac{1}{2\pi\sqrt{L_r C_r}}, \quad C_r = C_{\rm ra} + C_{\rm rb} + C_{\rm rc}. \tag{11}$$

The driving-point impedance $\dot{Z}_i$, including the series-resonant tank, in Fig. 8(b), can be expressed as

$$\dot{Z}_i = \frac{R_o}{(1-\omega_s{}^2 L_o C_p + \frac{C_p}{C_o})^2 + (\omega_s C_p R_o)^2} + j\left\{\left(\omega_s L_r - \frac{1}{\omega_s C_r}\right) + \frac{(\omega_s L_o - \frac{1}{\omega_s C_o})(1-\omega_s{}^2 L_o C_p + \frac{C_p}{C_o}) - \omega_s C_o R_o^2}{(1-\omega_s{}^2 L_o C_p + \frac{C_p}{C_o})^2 + (\omega_s C_p R_o)^2}\right\}. \tag{12}$$

The characteristics of the output impedance versus normalized frequency are depicted in Fig. 9 on the basis of (6), where the numerical examples are given as $R_o = 2.0\,\Omega$, $L_o = 50\,\mu$H, $C_p = 100$ nF, and $C_o = 50$ nF. Fig. 9 indicates that switching frequency f_s should be set close to the resonant frequency f_{r1}

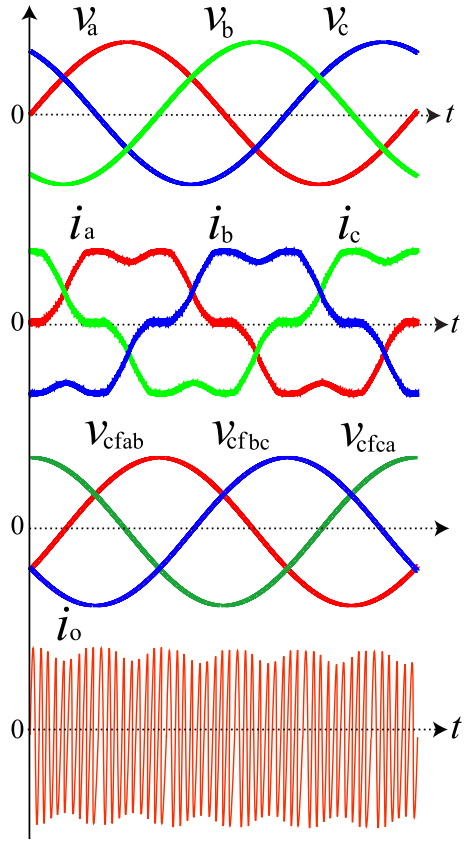

Fig. 10. Relevant voltage and current waveforms for an UFAC cycle.

under the heavy load condition, while close to f_{r2} under the light load condition owing to the effect of the parallel-resonant circuit; power regulation can be realized by PFM in the area between f_{r1} and f_{r2}. The maximum power $P_{\text{odel}_{\max}\max_{\max}}$ can be obtained at $f_s = f_{r1}$ whole the minimum power $P_{\text{odel}_{\min}\min}$ appears at $f_s = f_{\text{rs}}$, respectively. Therefore, the switching frequency f_s changes between $f_{r1} \leq f_s$ and $\leq f_{r2}$ for the output power regulation.

The switch conduction current i_s can be reduced as compared to the output current i_o. The rms current ratio λ of the two currents are defined as

$$\lambda = \frac{I_o}{I_s} = \frac{1}{\omega_s C_p \sqrt{R_o^2 + (\omega_s L_o + \frac{1}{\omega_s C_o} - \frac{1}{\omega_s C_p})^2}}. \quad (13)$$

In order to achieve ZCS turn-ON and ZVS turn-OFF commutations of the bidirectional switches, the lagging phase current is required for i_p. Therefore, the series-resonant frequency f_{rs} is designed to satisfy the following condition referring to Fig. 9 as

$$f_{\text{rs}} < f_{r1} \leq f_s \leq f_{r2}. \quad (14)$$

B. Operating Principle

The theoretical voltage and current waveforms for UFAC cycle of the proposed ac–ac converter are displayed in Fig. 10. The input currents i_a–i_c have the fifth harmonics of the utility frequency due to the two-phase switching modulation as discussed in Section II. It should be noted here that the voltages

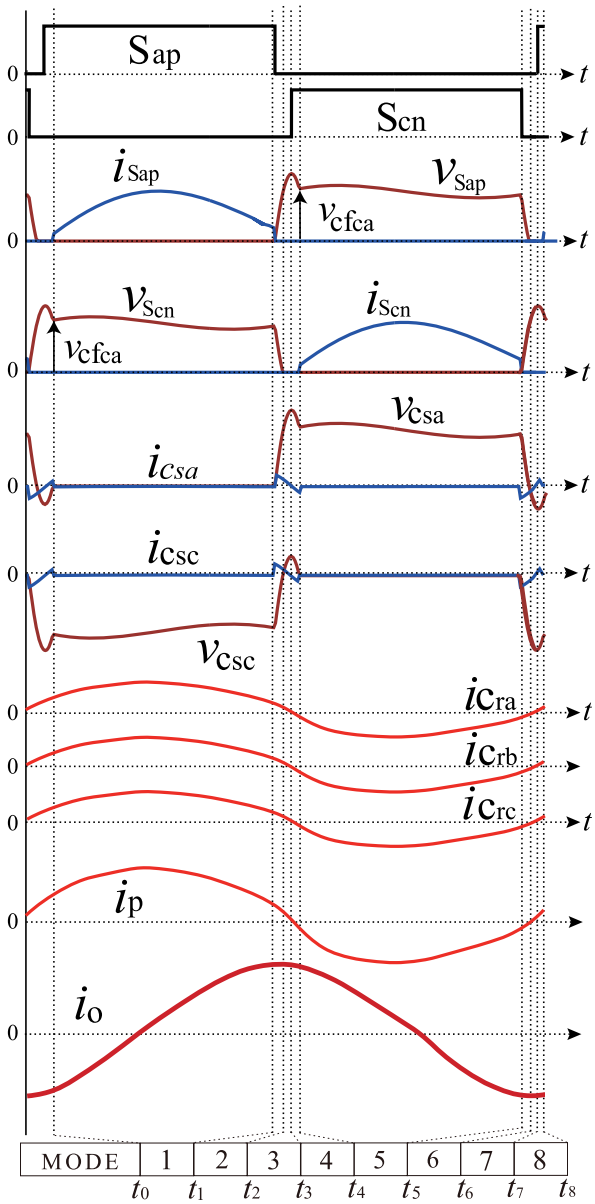

Fig. 11. Operating waveforms during the HFAC one cycle in the interval $v_a > v_b > 0 > v_c$.

of filter capacitor $v_{cf_{\text{ab}}}$–$v_{cf_{\text{ca}}}$ are approximately equal to the line voltage assuming that the voltage drop across the filter reactor can be ignored.

The operating waveforms and mode transitional equivalent circuits are depicted in Figs. 11 and 12 for the time interval of $v_a > v_b > 0 > v_c$. The operation mode is divided into the eight modes as follows.

1) Mode 1 (steady-state power transfer for the positive half cycle: $t_0 \leq t < t_1$). The active switch S_{ap} is ON-state, and the energy charged in the lossless snubber capacitor C_{sa} is zero. During this interval, the lossless snubber capacitor C_{sc} are negatively charged to the power supply side.
2) Mode 2 (ZVS turn-OFF transition in a positive switch of phase a : $t_1 \leq t < t_2$). The active switch S_{ap} is turned OFF at $t = t_1$, then the lossless snubber capacitors C_{sa}

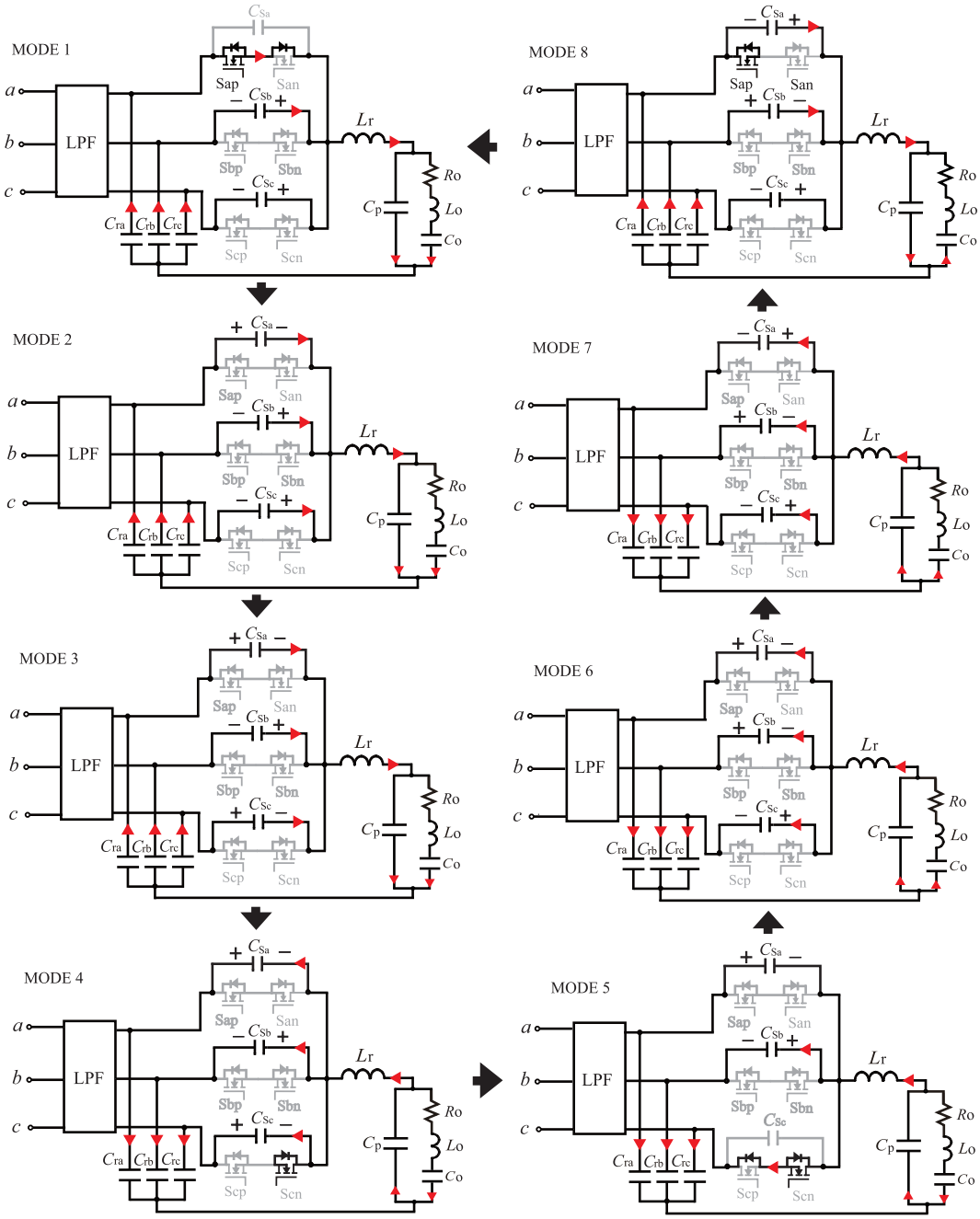

Fig. 12. Switching mode transitions for the UFAC interval $v_a > v_b > 0 > v_c$.

and inductance L_r make edge resonance. Accordingly, the voltage v_{sap} rises with a certain slope from zero, and the ZVS turn-OFF commutation starts in S_{ap}. Assumed the HF current i_p is equally shared among the three bidirectional switches, the condition of ZVS turn-OFF at S_{ap} can be expressed by

$$\frac{1}{6}L_r i_p(t_1)^2 > \frac{1}{2}C_{\text{sc}} v_{C\text{sc}}(t_1)^2. \tag{15}$$

3) Mode 3 (lossless snubber capacitor C_{sc} charging: $t_2 \leq t < t_3$). The lossless snubber capacitor C_{sc} is completely discharged at $t = t_2$; $v_{\text{Scn}}(t_2) = 0$ while $v_{\text{Sap}}(t_2) = v_{cf_{\text{ca}}} \simeq v_{\text{ca}}$. The lagging current i_p is equally divided into the three sets of lossless snubber capacitors and C_{sc} is charged to the power supply side. In this interval, the voltage of positive switch S_{ap} is expressed as

$$v_{\text{sap}}(t) = v_{\text{ca}} + \frac{1}{3C_{\text{sa}}}\int_{t_2}^{t} i_p d\tau.$$

4) Mode 4 (ZCS turn-ON in a negative switch of phase c: $t_3 \leq t < t_4$). The active switch S_{cn} is ON-state at $t = t_3$. The diode of the switch S_{cp} is reversely biased by the lossless snubber capacitor C_{sc}, and no current flows into the switch S_{cn}, whereby ZCS turn-ON can be performed.

Thus, taking the operation of Mode 7 into consideration, the condition of ZCS turn-ON of S_{ap} can be expressed by

$$v_{S_{\text{cn}}}(t_2) = 0, \quad i_{S_{\text{cn}}}(t_3) = 0. \tag{16}$$

During this interval, the primary side current of M.T. naturally reverses and discharges the lossless snubber capacitor C_{sc}. Accordingly, the voltage of S_{ap} drops to the line voltage v_{ca}.

5) Mode 5 (steady-state power transfer for the negative half cycle: $t_4 \le t < t_5$). After the lossless snubber capacitor C_{sc} has completely discharged, the primary current i_p of M.T. flows into the switch S_{cn}, then power is supplied to the IH load.
6) Mode 6 (ZVS turn-OFF in a negative switch of phase c: $t_5 \le t < t_6$). The active switch S_{cn} is turned OFF at $t = t_5$, then the voltage v_{scn} rises with a certain slope from zero, and the ZVS turn-OFF commutations starts in S_{cn} due to the edge resonance. Assumed the HF current i_p is equally shared among the three bidirectional switches, the condition of ZVS turn-OFF at S_{cn} can be defined as

$$\frac{1}{6}L_r i_p(t_5)^2 > \frac{1}{2}C_{\text{sa}} v_{C\text{sa}}(t_5)^2. \tag{17}$$

7) Mode 7 (lossless snubber capacitor C_{sa} charging: $t_6 \le t < t_7$). The lossless snubber capacitor C_{sa} is completely discharged at $t = t_6$; $v_{S_{\text{ap}}} = 0$ while $v_{\text{Scn}}(t_6) \simeq v_{\text{ca}}$. The lagging current is equally divided into the three sets of lossless snubber capacitors and the lossless snubber capacitor C_{sa} is negatively charged on the power supply side. During this interval, the voltage of active switch S_{cn} is obtained as

$$v_{\text{Scn}}(t) = v_{\text{ca}} + \frac{1}{3C_{\text{sc}}}\int_{t_6}^{t} i_p d\tau.$$

8) Mode 8 (ZCS turn-ON in a positive switch of phase a: $t_7 \le t < t_8$). The active switch S_{ap} is turned ON at $t = t_7$. At the same time, the diode of S_{an} is reversely biased and no current flows in S_{ap}, whereby the ZCS turn-ON can attain. Thus, taking the operation of Mode 7 into consideration, the condition of ZCS turn-ON of S_{ap} can be expressed by

$$v_{S_{\text{ap}}}(t_6) = 0, \quad i_{S_{\text{ap}}}(t_7) = 0. \tag{18}$$

The resonant current through L_r naturally reverses during this interval, and is equally divided into the three sets of lossless snubber capacitors. During this interval, the lossless snubber capacitor C_{sa} discharges while the voltage of S_{cn} drops to line voltage v_{ca}. The circuit operation gets back into Mode 1 and the repetitive next cycle begins.

III. Design Procedure of Circuit Parameters

A. Switching and Resonant Frequencies

The switching frequency f_s for an IH system depends on the material of the work piece to be heated. Skin depth or penetrating depth is also dependent on the switching frequency and material properties. Thus, the key point of the metal hardening IH system is to deliver the high-frequency power with the practical range of frequency.

A practical formula for skin depth δ mm is expressed as

$$\delta = 50.33\sqrt{\frac{\rho}{\mu_r f_s}} \tag{19}$$

where ρ is the resistivity of the material and μ_r is the absolute magnetic permeability [28]. The heated object is stainless steel bolts ($\mu_r = 1$ and $\rho = 72$), and the skin depth is designed 1.4–1.5 mm. The switching frequency at $\delta = 1.5$ mm is obtained from (19) as

$$f_s = 50.33^2\frac{\rho}{\mu_r \delta^2} \simeq 83\,\text{kHz}. \tag{20}$$

The first resonant frequency f_{r1} in (8) should be identical with the switching frequency for obtaining maximum output power. The second resonant frequency f_{r2} in (9) should be set close to f_{r1} considering the penetrating depth and the fluctuation of IH load parameter with frequency variation. As a consequence, f_{r2} is selected as 93 kHz at $\delta = 1.4$ mm, thereby the condition given in (14) can be satisfied.

B. Multiresonant Tank

The equivalent IH load inductance L_o and equivalent resistance R_o in the switching frequency range (83–93 kHz) are 2.0–2.1 Ω and 49–49.5 μH, respectively, from (4) and (5). Since the impedance variation in the switching frequency range is relatively small, the load resistance and inductance are determined as $L_o = 49\,\mu\text{H}$ and $R_o = 2.0\,\Omega$, respectively. Then, the output capacitor C_o can be determined from (8) at $f_s = f_{r1}$ as

$$C_o = \frac{1}{(2\pi f_{r1})^2 L_o} \simeq 75\,\text{nF}. \tag{21}$$

The parallel capacitor C_p can be obtained from (9) and (21) at $f_s = f_{r2}$ as

$$C_p = \frac{1}{(2\pi f_{r2})^2 L_o - \frac{1}{C_o}} \simeq 300\,\text{nF}. \tag{22}$$

C. Series-Resonant Tank

The lossless snubber capacitor C_s is selected as 3 nF to attain a low dv/dt rate sufficient for achieving the ZVS turn-OFF transitions at the bidirectional switches S_{ap}-S_{cn}. Then, the series-resonant inductance L_r can be determined from (15) and (17) as

$$L_r > \frac{3C_s {v_{Cs}}^2}{{i_{p_{\text{min}}}}^2} \simeq 22.5\,\mu\text{H} \tag{23}$$

where $i_{p_{\text{min}}}$ and v_{Cs} represent the switch turn-OFF current and voltage across the snubber capacitor, respectively. It should be remarked here that those values are given as $i_{p_{\text{min}}} = 4\,\text{A}$ and $v_{Cs} = 200\,\text{V}$ on the basis of simulation. As a result, the resonant inductor L_r can be designed as $25\,\mu\text{H}$ with consideration for (23).

The proposed converter requires the imaginary component of $\dot{Z}_i$ to be inductive (i.e., lagging phase available current) to achieve ZVS condition as

$$\text{Im}\{\dot{Z}_i\} > 0. \tag{24}$$

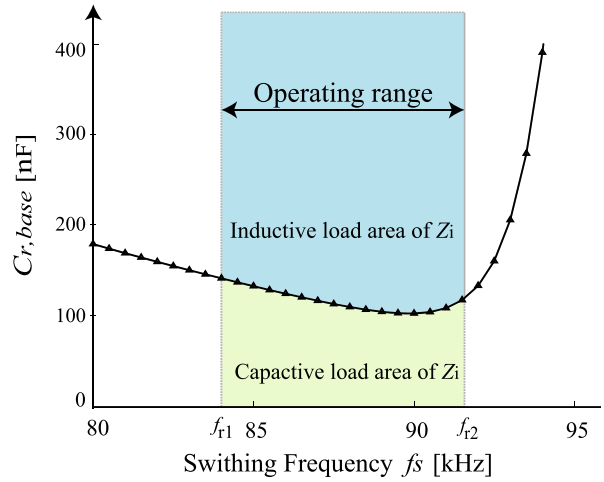

Fig. 13. Theoretical $C_{r,\text{base}}$ versus switching frequency.

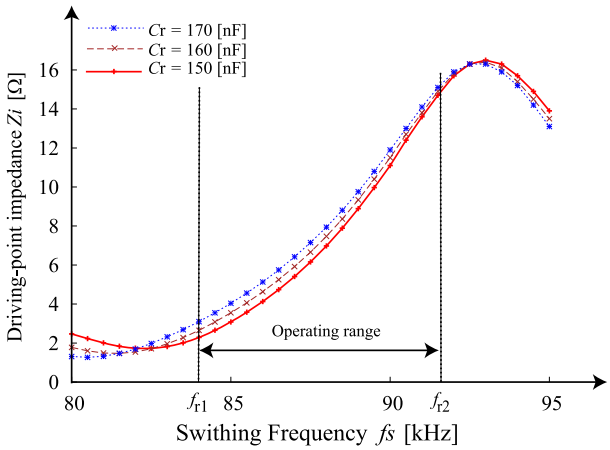

Fig. 14. Theoretical curve of the driving-point impedance versus switching frequency.

This results in

$$C_r > \frac{1}{\omega_s\left(\omega_s L_r + \text{Im}\{\dot{Z}_o\}\right)} = C_{r,\text{base}}. \tag{25}$$

Based on (25), the characteristics of $C_{r,\text{base}}$ versus switching frequency f_s is illustrated in Fig. 13. It can be understood from the curve that $C_{r,\text{base}}$ decreases as the switching frequency increases. Therefore, the series-resonant capacitor C_r must be designed to be higher than the maximum available value of the $C_{r,\text{base}}$, which can be calculated as 148 $n\Omega$ at $f_{r1} = 83$ kHz.

The calculation curves of the driving-point impedance Z_i and switching frequency are illustrated in Fig. 14 with the variations of C_r :150, 160, and 170 nF. It is recognizable that Z_i increases in proportion to C_r. Hence, C_r should be selected as 150 nF from the view point of maximum power available in the proposed converter.

D. Resonant Frequency Tracking Based on Phase-Locked Loop (PLL)

The resistive and inductive parameters (R_o–L_o) of the heated load varies when its temperature reaches the curie point.

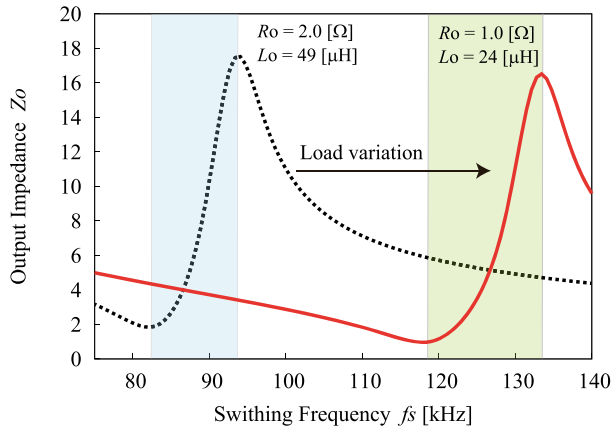

Fig. 15. Frequency-domain characteristics of the output impedance Z_o.

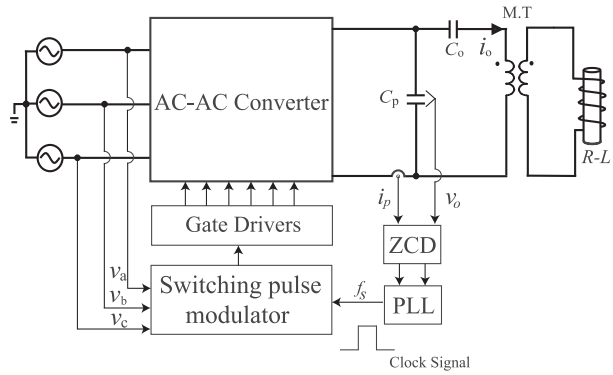

Fig. 16. Controller diagram with PLL and switching pulse modulator.

Fig. 15 depicts the transitional characteristics of the output impedance Z_o when R_o and L_o change from $R_o = 2.0\,\Omega$ and $L_o = 49\,\mu$H to $1.0\,\Omega$ and $24\,\mu$H as a numerical example, respectively. As depicted here, the resonant frequencies expressed in (8) and (9) change in principle. In addition, the switching frequency should be increased gradually in order to match with the resonant frequencies at the start-up process.

Fig. 16 shows the controller system that incorporates PLL as a subcontroller into the switching pulse modulator. In the high-frequency resonant converter, PLL is effective to adjust the switching frequency f_s by detecting the phase difference of current i_p and voltage v_o, thereby (14) can be satisfied while the designed parameters of the passive components remain. The output frequency targeted in the proposed converter is around 100 kHz, accordingly the PLL can be implemented with a general type of CMOS PLL-IC, e.g., CD4046B (Texas Instruments) [29].

IV. Experimental Results and Evaluations

The essential performances of the proposed direct ac–ac converter are verified by experiment of the 1.7-kW laboratory prototype at the switching frequency range 85–90 kHz. The exterior appearance of the prototype is indicated in Fig. 17. The circuit parameters and specifications that are described in Section III are listed in Table I. The bidirectional switches are implemented with a pair of series connection of two discrete Super

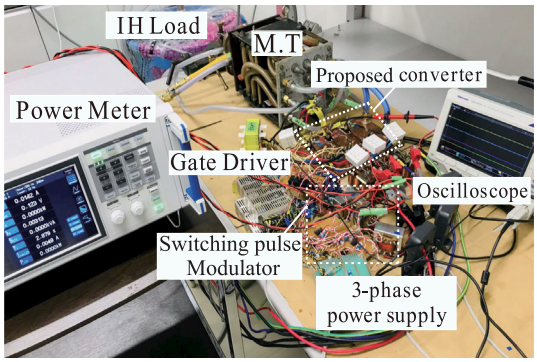

Fig. 17. Exterior appearance of prototype.

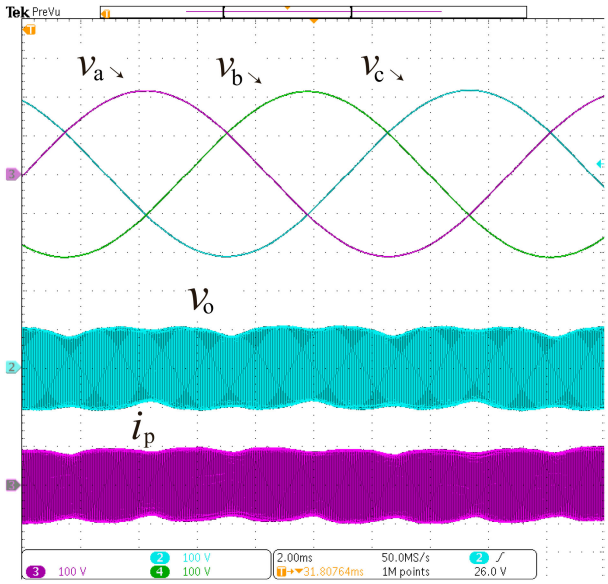

Fig. 18. Observed waveforms of three-phase utility voltages and primary-side voltage of M.T. at $P_o = 1.7\,\text{kW}$ with $f_s = 85\,\text{kHz}$ (v_a, v_b, v_c, v_o: 100 V/div, and i_p: 40 A/div, 2.0 ms/div).

Junction Si-MOSFETs (IXFN100N65X2: 650V-78A, $R_{\text{DS,on}} = 30\,\text{m}\Omega$). The resonant capacitors C_p and C_o are assembled by a high-frequency conduction-cooled power capacitor (CSM 150, Celem) in series and parallel connections, respectively. A stainless bolt bar is employed for the heated metal object. The M.T. and work-coils are water-cooled as well as the power devices.

A. *Operating Waveforms for UFAC and HFAC Cycles*

The observed waveforms of the three-phase source input and high-frequency output voltages and currents for the UFAC cycles are depicted in Fig. 18. The output waveform includes the component of six times as the switching frequency on the envelope due to the two-phase modulation, which selects the maximum- and minimum-phase voltages. Besides that, the HFAC current i_p is produced in the output of the direct ac–ac converter, thus, the direct ac–ac conversion is actually verified.

The switching voltage and current waveforms of a set of positive and negative phases are depicted in Fig. 19 at the point

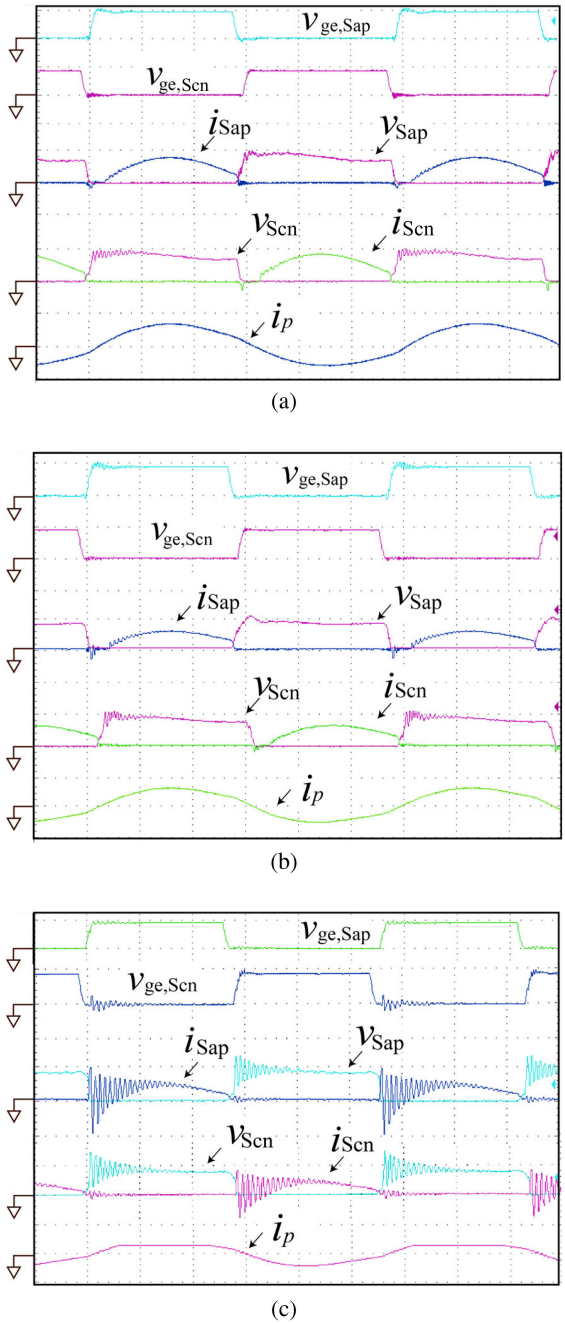

Fig. 19. Observed switching voltage and current waveforms of switches S_{ap}, S_{cn} and primary current of M.T i_p for a switching cycle at $v_a = 210\,\text{V}$: (a) $P_o = 1.7\,\text{kW}$, $f_s = 85\,\text{kHz}$, (b) $P_o = 1.0\,\text{kW}$, $f_s = 88\,\text{kHz}$, and (c) $P_o = 0.7\,\text{kW}$, $f_s = 90\,\text{kHz}$ ($v_{\text{sap}}, v_{\text{scn}}$: 250 V/div, $i_{\text{sap}}, i_{\text{scn}}$: 30 A/div, i_p: 40 A/div, 2 μs/div).

of the peak source voltage. The ZCS turn-ON and ZVS turn-OFF operations can be observed in S_{ap} and S_{cn} at $P_o = 1.0$–$1.7\,\text{kW}$ in Fig. 19(a) and (b). The voltages rise linearly at the turn-OFF transitions of S_{ap} and S_{cn}, respectively, thereby the overlapping areas of voltage and current are minimized due to the effect of lossless snubber capacitors. On the other hand, in the output power range between 0.7 and 1.0 kW, some volume of voltage remains at the turn-OFF transition in the lossless snubber capacitor as seen in Fig. 19(c). Accordingly, the capacitive energy of the lossless snubber is discharged through the active

TABLE I
EXPERIMENTAL CIRCUIT PARAMETERS

Item	Symbol	Value[unit]
UFAC source voltages	V_{ab},V_{bc},V_{ca}	150 [V]
Output power rating	P_o	1.7 [kW]
Utility frequency	f_u	60 [Hz]
Switching frequency	f_s	85-90 [kHz]
Utility filter capacitor	C_f	300 [nF]
Utility filter inductor	L_f	200 [μH]
Lossless snubber capacitors	C_s	3 [nF]
Series resonant capacitor	C_r	150 [nF]
Series resonant inductance	L_r	25 [μH]
Parallel resonant capacitor	C_p	300 [nF]
Output capacitor	C_o	75 [nF]
Windings turns ratio of M.T.	$a = w_1/w_2$	18/1
Equivalent resistance of IH Load	R_o	2 [Ω]
Equivalent inductance of IH Load	L_o	49 [μH]

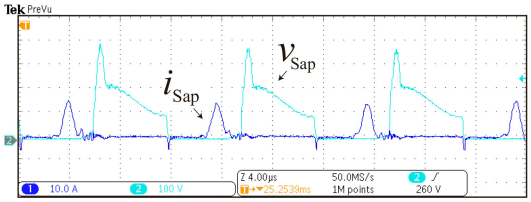

(a)

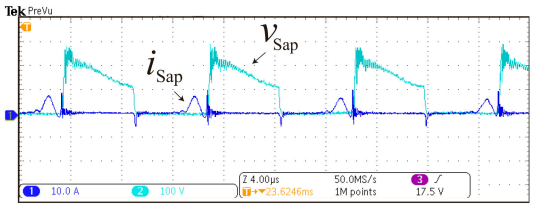

(b)

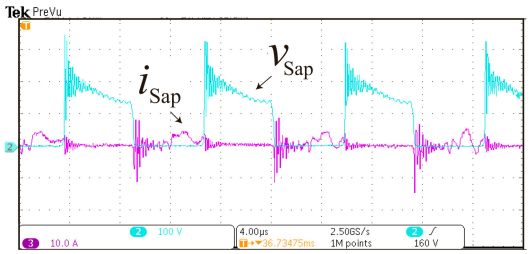

(c)

Fig. 20. Observed switching waveforms of S_{ap} and primary current of M.T i_p for a switching cycle at $v_a = 60$ V. (a) $P_o = 1.7$ kW, $f_s = 85$ kHz, (b) $P_o = 1.0$ kW, $f_s = 88$ kHz, and (c) $P_o = 0.7$ kW $f_s = 90$ kHz (v_{sap}, v_{scn}: 100 V/div, i_{sap}, i_{scn}: 10 A/div, 2 μs/div).

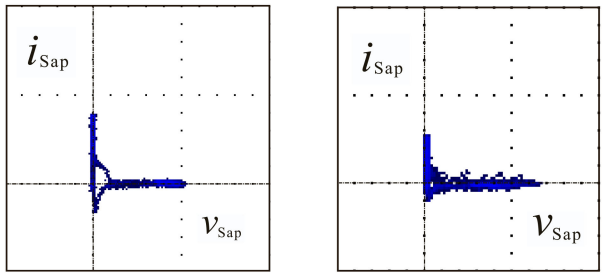

(a) (b)

Fig. 21. Lissajous figures of the active switch S_{ap} at $P_o = 1.7$ kW with $f_s = 85$ kHz. (a) Peak point of $v_a = 210$ V, and (b) low voltage of $v_a = 60$ V (v_{sap}: 250 V/div, i_{sap}: 30 A/div).

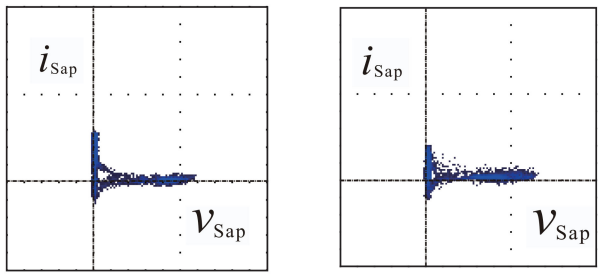

(a) (b)

Fig. 22. Lissajous figures of the active switch S_{ap} at $P_o = 1.0$ kW with $f_s = 88$ kHz. (a) Peak point of $v_a = 210$ V, and (b) low-voltage level of $v_a = 60$ V (v_{sap}: 250 V/div, i_{sap}: 30 A/div).

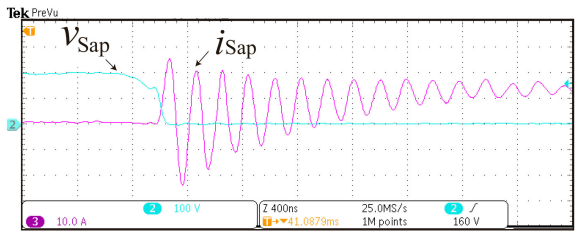

(a)

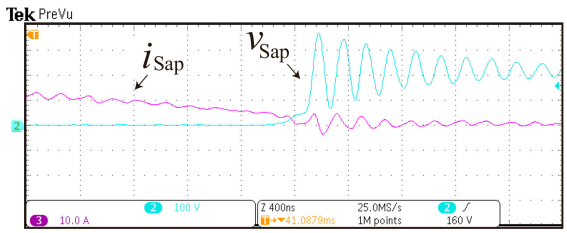

(b)

Fig. 23. Enlarged waveforms of S_{ap} at $P_o = 0.7$ kW with $f_s = 90$ kHz and $v_a = 210$ V. (a) Turn-ON and (b) turn-OFF transitions (v_{sap}: 100 V/div, i_{sap}: 10 A/div, 400 ns/div).

switch at turn-ON transitions in the next switching cycle. Fig. 20 shows the switching performances of S_{ap} at the medium voltage ($v_a = 60$ V) in the power settings identical to Fig. 19. It can be understood from Figs. 19(a) and (b) and 20(a) and (b) that the soft switching can attain in the middle to heavy load conditions regardless of the source voltage level while the incomplete soft commutation emerges at the light load.

The voltage–current trajectories are revealed in Figs. 21 and 22 for the heavy and middle loads in accordance with the source voltage level. It can be observed herein that the overlapping areas of voltage and current are minimized: thus, the soft commutation of the bidirectional switch is clearly verified in the middle and heavy load power settings.

In contrast to the middle and heavy loads, the incomplete soft switching emerges under the condition of light load as demonstrated in Figs. 19(c) and 20(c). In order to monitor the behavior with the light load, the enlarged waveforms at the

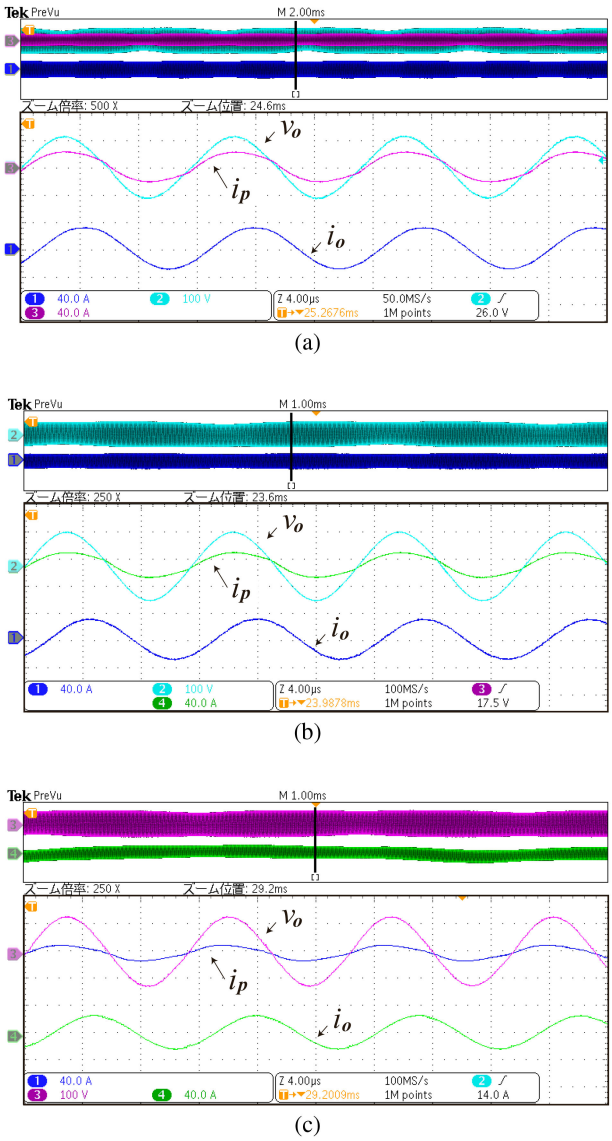

Fig. 24. Observed voltage and current waveforms of the multiresonant tank with IH load. (a) $P_o = 1.7\,\mathrm{kW}$, $f_s = 85\,\mathrm{kHz}$, (b) $P_o = 1.0\,\mathrm{kW}$, $f_s = 88\,\mathrm{kHz}$, and (c) $P_o = 0.7\,\mathrm{kW}$, $f_s = 90\,\mathrm{kHz}$ (i_p, i_o: 40 A/div, v_o: 100 V/div, $4\,\mu\mathrm{s/div}$).

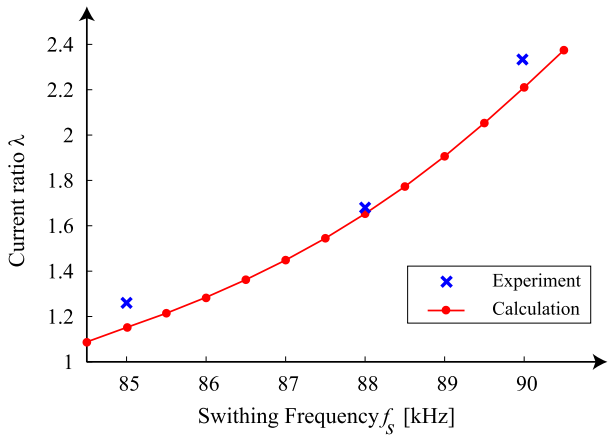

Fig. 25. Current ratio versus switching frequency.

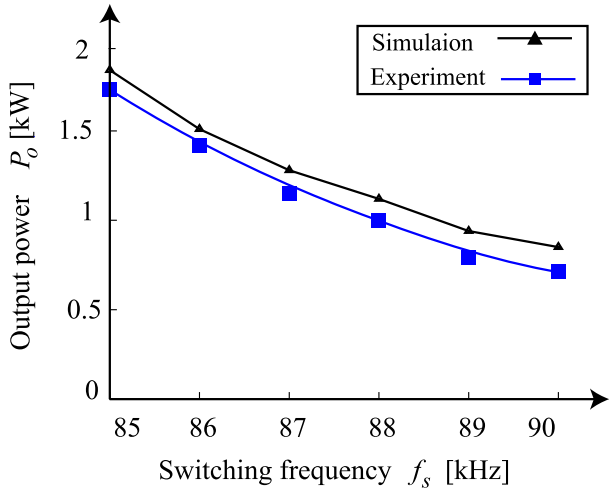

Fig. 26. Measured steady-state characteristics of output power regulation versus switching frequency under the open-loop control.

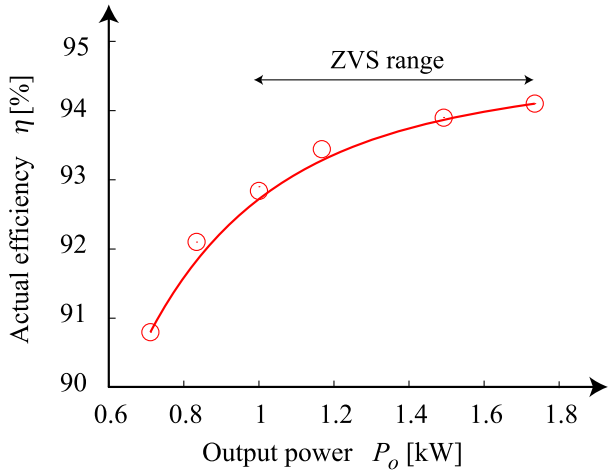

Fig. 27. Actual efficiency versus output power curve (power meter: HIOKI-PW6001).

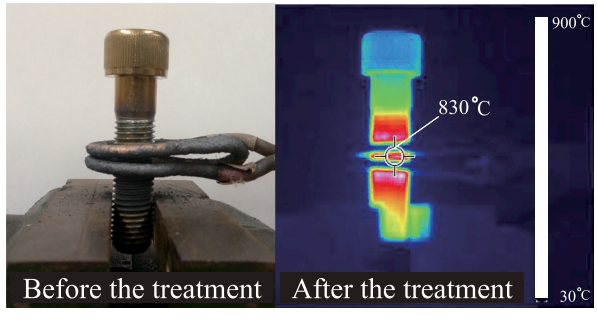

Fig. 28. Appearances of the heated metal load.

turn-ON and -OFF transitions are depicted in Fig. 23. The ringings appear in the switching current $i_{S_{\mathrm{ap}}}$ at the turn-ON transitions while the voltage $v_{S_{\mathrm{ap}}}$ goes down to zero and keeps the state, accordingly the ZCS condition in (18) is partly satisfied and no power dissipation occurs. The ringings appear both in $i_{S_{\mathrm{ap}}}$ and

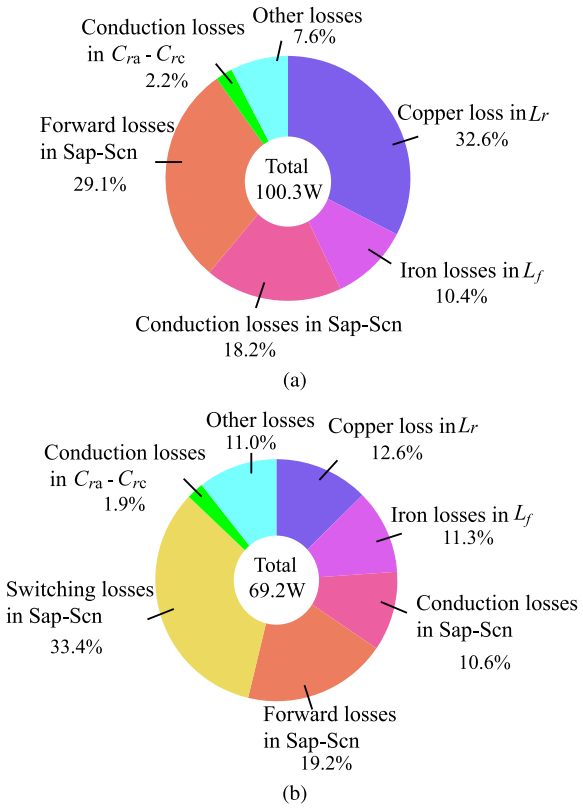

Fig. 29. Power-loss analysis. (a) $P_o = 1.7\,\text{kW}$, $f_s = 85\,\text{kHz}$ and (b) $f_s = 90\,\text{kHz}$, $P_o = 0.7\,\text{kW}$.

$v_{S_{\text{ap}}}$ at the turn-OFF transition, then power loss emerges at each switch.

The voltage and current waveforms of the multiresonant tank with IH load are depicted in Fig. 24. The multiresonant tank input current i_p is well regulated lower than i_o at the primary-side M.T., which corresponds with the load current over the wide range of output power. Thus, the validity of the multiresonant tank in the proposed converter is clearly revealed.

The experimental results and calculation values of the current ratio λ obtained from (13) with the circuit parameters in Table I are shown in Fig. 25. As f_s increases, the current ratio λ increases by the effect of multi resonant tank that maintains a high amplitude of load current even in the light load condition. The measured results indicate that the experimental values agrees with the calculated ones that are based on (13), thereby effectiveness of the design process introduced in Section III is verified.

B. Steady-State Characteristics

The output power characteristics are displayed under the open-loop control in Fig. 26, which exhibit the PFM-based power regulation for the proposed ac–ac converter. It can be confirmed that the PFM scheme is effective for the HF output power regulation with the smaller frequency variation of 85–90 kHz, consequently the minimum output power is obtained as 0.7 kW (41% load setting) at $f_s = 90\,\text{kHz}$. The ZVS operation can be accomplished in the three sets of bidirectional switches in the output power range between 1.0 and 1.7 kW (58%–100% load settings).

The actual efficiency of the ac–ac power conversion is depicted in Fig. 27. The output power is measured by including the power losses in the resonant capacitors C_p and C_o, which can be ignored due to the low equivalent series resistance; 3 $m\Omega$ and 9 $m\Omega$ in blocks, respectively. The maximum efficiency attains 94.1% at $P_o = 1.7\,\text{kW}$ in the proposed prototype, and high efficiency over 90% can be maintained in the power range 0.7–1.7 kW.

Fig. 28 shows the appearance of the metal bolt before and after injecting the high-frequency power. The temperature distribution of the heated load is visualized by the thermography during the surface heating. The surface temperature of the heated bolt rises up to 830 °C that is enough for hardening, thus, the successful metal-surface-treatment is actually verified by those thermal images.

The power losses of the prototype are analyzed according to the output power level. The power losses in the bidirectional switches are main concern in the loss analysis, accordingly the conduction and switching losses are defined and calculated as follows: The conduction loss $P_{\text{sw,cond}}$ and the forward conduction loss $P_{\text{sw,forward}}$ of each of the six discrete switch S_{ap}-S_{cn} are calculated by using the following formulas as

$$P_{\text{sw,cond}} = 2f_s \left(\int_{t_0}^{t_1} R_{\text{DS,on}} {i_{\text{DS}}}^2 dt \right) \tag{26}$$

$$P_{\text{sw,forward}} = 2f_s \left(\int_{t_0}^{t_1} v_{\text{DS}} i_{\text{DS}} dt \right) \tag{27}$$

where v_{DS}, i_{DS}, and $R_{\text{DS,on}}$ denote the forward conduction voltage, current, and on-resistance of each switch, respectively. Note here the time interval t_0–t_1 corresponds to the duration of Mode 1 in Fig. 11. In addition, the switching loss P_{sw}, especially the turn-OFF loss in S_{ap}-S_{cn} is defined and calculated by approximating v_{DS} and i_{DS} with a linear function as expressed by

$$P_{\text{sw}} = \int_0^{T_{\text{sw,off}}} v_{\text{DS}} i_{\text{DS}} f_s dt \tag{28}$$

where $T_{\text{sw,off}}$ represents a turn-OFF transition of each switch.

The power loss breakdowns of the direct ac–ac power conversion stage are revealed in Fig. 29. It can be understood from the analysis that the copper loss of L_r and forward conduction losses of the discrete power MOSFETs account for a large part of the total loss, especially in the heavy load setting $P_o = 1.7\,\text{kW}$. The forward conduction losses might be reduced by integrating a silicon carbide schottky barrier diode into each discrete switch for reducing a reversely conduction voltage drop V_{SD}. The switching loss related to the turn-OFF ringings emerge in the low output power setting $P_o = 0.7\,\text{kW}$ as discussed earlier. In order to mitigate the ringings and reduce the relevant power losses under the condition of light load, employment of alternative pulse modulation such as pulse density modulation (PDM) may be an effective solution while paying for a complicated control algorithm and a low-frequency subharmonics [30].

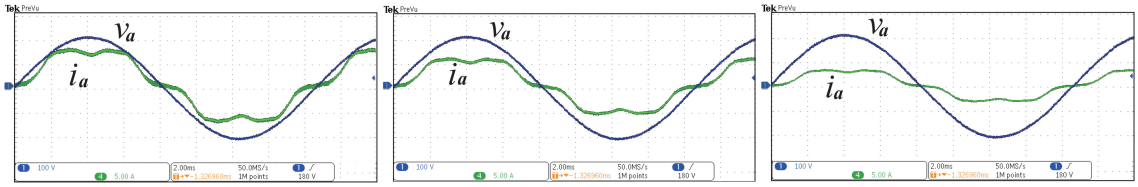

Fig. 30. Observed input voltage v_a and current i_a waveforms of the utility power source. (a) $P_o = 1.7\,\text{kW}$, $f_s = 85\,\text{kHz}$, (b) $P_o = 1.0\,\text{kW}$, $f_s = 88\,\text{kHz}$, and (c) $P_o = 0.7\,\text{kW}$, $f_s = 90\,\text{kHz}$ (100 V/div, 5 A/div, 2.0 ms/div).

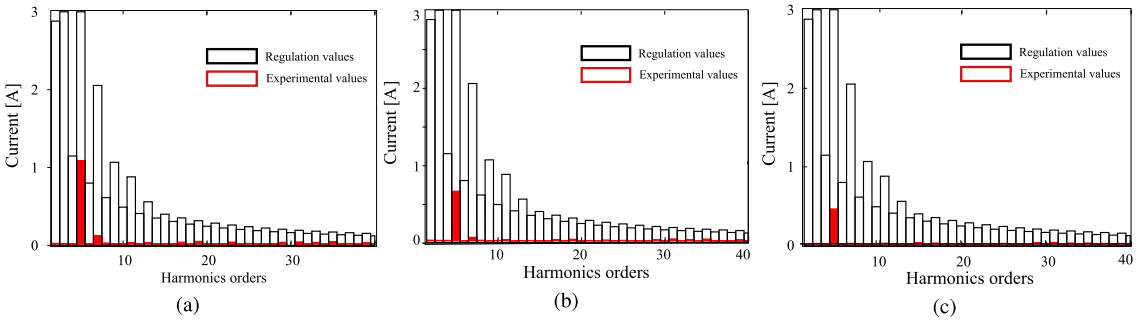

Fig. 31. Harmonics analysis of UFAC line current i_a. (a) $f_s = 85\,\text{kHz}$, $P_o = 1.7\,\text{kW}$, (b) $f_s = 88\,\text{kHz}$, $P_o = 1.0\,\text{kW}$, and (c) $f_s = 90\,\text{kHz}$, $P_o = 0.7\,\text{kW}$.

TABLE II
COMPARISON OF THREE-PHASE TO SINGLE-PHASE AC–AC CONVERTERS FOR HIGH-FREQUENCY IH AND IPT APPLICATIONS

Circuit Topology	Switch counts*	Switching frequency	DC-link Filter	PFC	Voltage stress v_{sw} Current ratio $\lambda^{\dagger}$	S-SW Efficiency	Modulation Algorithm
Thyristor rectifier VS HF-INV[3] (see Fig.3 (a))	10	100-400 kHz @HF-INV	bulky, short-cycle	low	$v_{sw} = V_{dc}$ $\lambda = 1$	ZVS 95 %@100 kW	PFM simple
Thyristor rectifier CS HF-INV[5] (see Fig.3 (b))	10	20 kHz @HF-INV	large&heavy	low	$v_{sw} = QI_o$ $\lambda > 1$	ZCS NR	PWM / PFM simple
PWM converter VS HF-INV (see Fig.3 (c))	10	20-50 kHz @HF-INV	bulky, short-cycle	high	$v_{sw} = v_{in}$ $\lambda = 1$	ZVS 91-95 % (estimated)	PWM / PFM complicated
Full HF-MC (see Fig. 4(a))[14]	12	174 kHz	None	high	$v_{sw} = v_{in}$ $\lambda = 1$	ZVS 92 %@2 kW	PWM&PDM complicated
RB-IGBT based half HF-MC[15]	7	12.3 kHz	None	medium	$v_{sw} = v_{in}$ $\lambda = 1$	ZCS 87.9 %@140 W	PFM complicated
A SiC-based half HF-MC[16]	8	50 kHz	None	medium	$v_{sw} = v_{in}$ $\lambda = 1$	NR 85 %@300 W	PS-PWM‡ complicated
Phase-modular HF-MC (see Fig. 4(b))[26]	12	20 kHz	None	high	$v_{sw} = 2v_{in}$ $\lambda > 1$	ZVS&ZCS 93 %@8 kW	PWM&PDM complicated
Proposed converter	6	85-90 kHz	None	medium	$v_{sw} = v_{in}$ $\lambda = 1.3$-2.4	ZVS&ZCS 94.1 %@1.7 kW	PFM simple

*Counted by a discrete power device. † See (13) ‡ PS: Phase-shift.

C. Harmonics Analysis of UFAC Line Current

The observed three-phase source voltage and current waveforms are provided in Fig. 30 in accordance with the output power settings. The total power factors are observed over 96% with the power analyzer HIOKI-PW6001. Thus, the high performance of the proposed converter is actually demonstrated from the view point of a power electronics interface the utility power.

The line current harmonics analysis corresponding to Fig. 30 is depicted in Fig. 31, where the measured values are compared with the reference standards of IEC61000-3-2-Class A. The input line currents include some fifth harmonics due to the two-phase switching modulation. However, the distortions of the line currents also clear the guideline of the industrial factories IEEE519, which recommends installation of an active power filter in the power feeder of a factory. Otherwise, the auxiliary circuit will be necessary in the rear-end half HF-MC or pulsewidth modulation (PWM) rectifier in a front-end stage [31], [32], both of which are not practical nor a better solution instead of installing an active or passive filter in the power feeder line of the factory [33]–[35].

D. Comparison With Existing Converters

Table II summarizes the performances of the existing three-phase to single-phase ac–ac converters and proposed converter. It should be remarked herewith that efficiencies are to be compared under the same power level while all the information in this table are just originated from the reference papers.

The proposed converter is advantageous over the conventional thyristor rectifier and CS HF-INV / VS HF-INV in all the items of evaluation. It might fall behind the PWM rectifier-applied VS HF-INV and full HF-MC in terms of PFC performances. However, the proposed converter exhibits more excellent performances on the reduction of conduction currents and the relevant power losses, simplicity of pulse modulation and controller algorithm, and last but not least cost-effectiveness in power devices. The effectiveness of the multiresonant tanks in the proposed converter is verified by comparison with the half HF-MC with a series or series–parallel resonant tanks.

V. Conclusion

The newly developed three-phase ac to single-phase ac direct converter suitable for the industrial high-frequency IH applications has been presented in this article.

Three sets of bidirectional switches operate under the two-phase modulation, and achieve soft switching over the wide range of source voltage without any dc-link large-volume capacitor. The multiresonant tank for the IH load contributes for the reduction of the switch conduction current while high resonant current with low distortion generates in the output stage and the heated metal load. The design guideline of the circuit parameters has been described step by step, taking the power regulation and soft-switching range into consideration.

The direct three-phase UFAC to single-phase HFAC conversion has been revealed as well as the practically accepted low distortion of line current and high total power factor in the experiment. The power conversion efficiency has been confirmed over 94% with the ZVS and the incomplete ZVS operations in the output power setting of 0.7–$1.7\,\mathrm{kW}$ (41%–100%) with 85–$90\,\mathrm{kHz}$. The total power factor has been measured over 96% in the utility line currents, which proves the effectiveness of the proposed converter as a utility-interfaced power supply.

It has been originally demonstrated that the proposed ac–ac converter contributes for technical improvements of industrial induction heaters in terms of the compactness, cost-effectiveness, high efficiency and long life cycle.

References

[1] H. Fujita and H. Akagi, "Pulse-density-modulated power control of a 4 kW, 450 kHz voltage-source inverter for induction melting applications," *IEEE Trans. Ind. Appl.*, vol. 32, no. 2, pp. 279–286, Mar./Apr. 1996.

[2] V. Esteve, J. Jordán, E. Sanchis-Kilders, E. Dede, E. Maset, and J. B. Ejea, "Enhanced pulse-density-modulated power control for high-frequency induction heating Inverters," *IEEE Trans. Ind. Electron.*, vol. 62, no. 11, pp. 6905–6914, May 2015.

[3] A. Okuno, H. Kawano, J. Sun, M. Kurokawa, A. Kojina, and M. Nakaoka, "Feasible development of soft-switched SIT inverter with load-adaptive frequency-tracking control scheme for induction heating," *IEEE Trans. Ind. Appl.*, vol. 34, no. 4, pp. 713–718, Jul./Aug. 1998.

[4] T. Mishima, S. Sakamoto, and C. Ide, "ZVS phase-shift PWM-controlled single-stage boost full-bridge ac-ac converter for high-frequency induction heating applications," *IEEE Trans. Ind. Electron.*, vol. 64, no. 3, pp. 2054–2061, Mar. 2017.

[5] A. Shenkman, B. Axelrod, and V. Chudnovsky, "Assuring continuous input current using a smoothing reactor in a thyristor frequency converter for induction metal melting and heating applications," *IEEE Trans. Ind. Electron.*, vol. 48, no. 6, pp. 1290–1292, Dec. 2001.

[6] V. Esteve "Improving the reliability of series resonant inverters for induction heating applications," *IEEE Trans. Ind. Electron.*, vol. 61, no. 5, pp. 2564–2572, May 2014.

[7] P. W. Wheeler, J. Rodriguez, J. C. Clare, L. Empringham, and A. Weinstein, "Matrix converters: A technology review," *IEEE Trans. Ind. Electron.*, vol. 49, no. 2, pp. 276–288, Apr. 2002.

[8] J. W. Kolar, T. Friedli, J. Rodriguez, and P. W. Wheeler, "Review of three-phase PWM ac-ac converter topologies," *IEEE Trans. Ind. Electron.*, vol. 58, no. 11, pp. 4988–5006, Jun. 2011.

[9] K. Koiwa and J. Itoh, "A maximum power density design method for nine switches matrix converter using SiC-MOSFET," *IEEE Trans. Power Electron.*, vol. 31, no. 2, pp. 1189–1202, Feb. 2016.

[10] E. Afshari, M. Khodabandeh, and M. Amirabadi, "A single-stage capacitive ac-link ac-ac power converter," *IEEE Trans. Power Electron.*, vol. 34, no. 3, pp. 2104–2118, Mar. 2019.

[11] M. Kazerani, "A direct ac/ac converter based on current-source converter modules," *IEEE Trans. Ind. Electron.*, vol. 18, no. 5, pp. 1168–1175, Sep. 2003.

[12] S. B. Dewan and G. Havas, "A solid-state supply for induction heating and melting," *IEEE Trans. Ind. General Appl.*, vol. IGA-5, no. 6, pp. 686–692, Nov./Dec. 1969.

[13] Y. Kim, S. Okuma, and K. Iwata, "Characteristics and starting method of a cycloconverter with a tank circuit for induction heating," *IEEE Trans. Power Electron.*, vol. 3, no. 2, pp. 236–244, Apr. 1988.

[14] N. Nguyen-Quang, D. A. Stone, C. M. Bingham, and M. P. Foster, "A three-phase to single-phase matrix converter for high-frequency induction heating," in *Proc. 13th Eur. Conf. Power Electron. Appl.*, 2009, pp. 1–10.

[15] M. Moghaddami, A. Anzalchi, and A. I. Sarwat, "Single-stage three-phase ac-ac matrix converter for inductive power transfer systems," *IEEE Trans. Ind. Electron.*, vol. 63, no. 10, pp. 6613–6622, Oct. 2016.

[16] N. X. Bac, D. M. Vilathgamuwa, and U. K. Madawala, "A SiC-Based Matrix converter topology for inductive power transfer system," *IEEE Trans. Ind. Electron.*, vol. 29, no. 8, pp. 4029–4038, Nov. 2013.

[17] H. Sugimura, S. P. Mun, S.-K. Kwon, T. Mishima, and M. Nakaoka, "High-frequency resonant matrix converter using one-chip reverse blocking IGBT-Based bidirectional switches for induction heating," in *Proc. IEEE Power Electron. Spec. Conf.*, 2008, pp. 3960–3966.

[18] H. L. Li, A. P. Hu, and G. A. Covic, "A direct ac-ac converter for inductive power-transfer systems," *IEEE Trans. Power Electron.*, vol. 27, no. 2, pp. 661–668, Feb. 2012.

[19] Ó. Lucia, C. Carretero, J. M. Burdio, J. Acero, and F. Almazan, "Multiple-output resonant matrix converter for multiple induction heaters," *IEEE Trans. Ind. Appl.*, vol. 48, no. 4, pp. 1387–1396, Jul./Aug. 2012.

[20] S. Komeda and H. Fujita, " A phase-shift-controlled direct ac-to-ac converter for induction heaters," *IEEE Trans. Power Electron.*, vol. 33, no. 5, pp. 4115–4124, May 2018.

[21] H. F. Ahmed, H. Cha, A. A. Khan, J. Kim, and J. Cho, "A single-phase buck-boost matrix converter with only six switches and without commutation problem," *IEEE Trans. Power Electron.*, vol. 32, no. 2, pp. 1232–1244, Feb. 2017.

[22] C. Liu "Novel bipolar-type direct ac-ac converter topology based on non-differential ac choppers," *IEEE Trans. Ind. Electron.*, vol. 34, no. 10, pp. 9585–9599, Oct. 2019.

[23] K. You, D. Xiao, M. F. Rahman, and M. N. Uddin, "Applying reduced general direct space vector modulation approach of ac-ac matrix converter theory to achieve direct power factor controlled three-phase ac-dc matrix rectifier," *IEEE Trans. Ind. Appl.*, vol. 58, no. 11, pp. 4988–5006, Jun. 2011.

[24] M. A. Sayed, K. Suzuki, T. Takeshita, and W. Kitagawa, "PWM switching technique for three-phase bidirectional grid-tie DC-AC-AC converter with high-frequency isolation," *IEEE Trans. Power Electron.*, vol. 33, no. 1, pp. 845–858, Jan. 2018.

[25] A. K. Singh, E. Jeyasankar, P. Das, and S. K. Panda, "A matrix-based nonisolated three-phase ac-dc rectifier with large step-down voltage gain," *IEEE Trans. Power Electron.*, vol. 32, no. 6, pp. 4796–4811, Jun. 2017.

[26] N. A. Ahmed, "High-frequency soft-switching ac conversion circuit with dual-mode PWM/PDM control strategy for high-power IH applications," *IEEE Trans. Ind. Electron.*, vol. 58, no. 4, pp. 1440–1448, May 2011.

[27] T. Mishima, R. Kawashima, and C. Ide, "Three-phase ac to single-phase ac multi-resonant direct converter for metal hardening high-frequency induction heater," in *Proc. 11th IEEE Energ. Covers. Congr. Expo.*, Sep./Oct. 2019, pp. 5472–5478.

[28] E. J. Davies, and P. G. Simpson, "Induction heating for industry," *Electron. Power.*, vol. 25, no. 7, pp. 508–515, Jul. 1979.

[29] M. Kamli, S. Yamamoto, and M. Abe, "A 50–150 kHz half-bridge inverter for induction heating applications," *IEEE Trans. Ind. Electron.*, vol. 43, no. 1, pp. 163–172, Feb. 1996.
[30] T. Mishima and M. Nakaoka, "A load-power adaptive dual pulse modulated current phasor-controlled ZVS high-frequency resonant inverter for induction heating applications," *IEEE Trans. Power Electron.*, vol. 29, no. 8, pp. 3864–3880, Aug. 2014.
[31] I. Wallace, A. Bendre, J. P. Nord, and G. Venkataramanan, "A unity-power-factor three-phase PWM SCR rectifier for high-power applications in the metal industry," *IEEE Trans. Ind. Appl.*, vol. 38, no. 4, pp. 898–908, Jul./Aug. 2002.
[32] M. Goh, S. Choi, J. Yu, and I. Kim, "High power factor induction heating power supply for forging applications using three-phase three-switch PWM current source rectifier," in *Proc. 22nd Int. Conf. Elect. Mach. Syst.*, Harbin, China, 2019, pp. 1–5.
[33] J. Titus, H. K. P and K. Hatua, "An SCR based CSI-Fed induction motor drive for high power medium voltage applications," *IEEE Trans. Ind. Electron.*, to be published, doi: 10.1109/TIE.2020.2988216.
[34] R. Sebastian and P. P. Rajeevan, "Load-commutated SCR-based current source inverter fed induction motor drive with open-end stator windings," *IEEE Trans. Ind. Electron.*, vol. 65, no. 3, pp. 2031–2038, Mar. 2018.
[35] D. Banerjee and V. T. Ranganathan, "Load-Commutated SCR current-source-inverter-fed induction motor drive with sinusoidal motor voltage and current," *IEEE Trans. Power Electron.*, vol. 24, no. 4, pp. 1048–1061, Apr. 2009.

Ryosuke Kawashima received the B.S. and M.S. degrees in maritime science from Kobe University, Kobe, Japan, in 2018 and 2020, respectively.

He mastered an internship program on the metal hardening induction heating applications with Fuji Electronics Industry Company LTD, Osaka, Japan, in 2018. He currently engages in research works and developments of Building Energy Management System (BEMS) for an architectural design company in Tokyo. His main research interests include the high-frequency inverter and resonant converter applications for industrial induction heatings systems.

Mr. Kawashima has been a Student Member of The Institute of Electrical Engineering of Japan (IEEJ) from 2018 to 2020.

Tomokazu Mishima (Senior Member, IEEE) received the B.S., M.S., and Ph.D. degrees in electrical engineering from The University of Tokushima, Tokushima, Japan, in 1999, 2001, and 2004, respectively.

Since 2010, he has been with Kobe University, Hyogo, Japan, as an Associate Professor, and engages in the research works and developments of power electronics circuits and systems. His research interests include soft-switching dc–dc converters, resonant converters, and high-frequency inverters for industrial, automotive, biomedical, renewable, and sustainable energy applications.

Dr. Mishima is the recipient of the Best Paper Award in the *Eighth* IEEE International Conference on Power Electronics and Drive Systems in 2009, the Best Paper Presentation Award of the Annual Conference of the IEEE Industrial Electronics Society (IECON) in 2012, and the IEEE TRANSACTIONS ON POWER ELECTRONICS Outstanding Reviewer Award, in 2017. He is currently an Associate Editor of the IEEE TRANSACTIONS ON POWER ELECTRONICS and a Secretary of *IEEJ Transactions on Industry Applications*. He is a Senior Member of IEEJ, and a member of The Institute of Electronics, Information and Communication Engineers, and Japan Institute of Power Electronics.

Chiaki Ide received the B.S. degree in electronics engineering from Yamanashi University, Kofu, Japan, in 1971.

He joined Fuji Electronics Industry Co. Ltd, Osaka, Japan, where he was the Director of the Manufacturing Department from 2008 to 2019, and is currently an Advisor. He has been engaged with the design and development of high-frequency induction heating facilities for metal surface treatments as well as the relevant inverter circuits.

Mr. Ide was the recipient of the 6th Monozukuri (Manufacturing) Nippon Grand Award by the Japanese Ministry of Economy, Trade, and Industry (METI) in 2015.